The Astrophysical Journal, 777:167 (10pp), 2013 November 10 doi:10.1088/0004-637X/777/2/167

ESTABLISHING A STEREOSCOPIC TECHNIQUE FOR DETERMINING THE KINEMATIC PROPERTIES OF SOLAR WIND TRANSIENTS BASED ON A GENERALIZED SELF-SIMILARLY EXPANDING CIRCULAR GEOMETRY

J. A. Davies[1], C. H. Perry[1], R. M. G. M. Trines[2,3], R. A. Harrison[1], N. Lugaz[4], C. Möstl[5,6,7], Y. D. Liu[8], and K. Steed[9]
[1] RAL Space, Rutherford Appleton Laboratory, Harwell Oxford, OX11 0QX, UK; jackie.davies@stfc.ac.uk
[2] Central Laser Facility, Rutherford Appleton Laboratory, Harwell Oxford, OX11 0QX, UK
[3] Department of Physics, Lancaster University, Lancaster LA1 4YB, UK
[4] Space Science Centre, University of New Hampshire, Durham, NH 03824, USA
[5] Space Science Laboratory, University of California, Berkeley, CA 94720, USA
[6] Institute of Physics, University of Graz, Graz A-8042, Austria
[7] Space Research Institute, Austrian Academy of Sciences, A-8042 Graz, Austria
[8] State Key Laboratory of Space Weather, National Space Science Centre, Chinese Academy of Sciences, Beijing 100190, China
[9] Centre for mathematical Plasma Astrophysics, KU Leuven, B-3001 Leuven, Belgium
Received 2013 March 1; accepted 2013 September 20; published 2013 October 24

ABSTRACT

The twin-spacecraft *STEREO* mission has enabled simultaneous white-light imaging of the solar corona and inner heliosphere from multiple vantage points. This has led to the development of numerous stereoscopic techniques to investigate the three-dimensional structure and kinematics of solar wind transients such as coronal mass ejections (CMEs). Two such methods—triangulation and the tangent to a sphere—can be used to determine time profiles of the propagation direction and radial distance (and thereby radial speed) of a solar wind transient as it travels through the inner heliosphere, based on its time-elongation profile viewed by two observers. These techniques are founded on the assumption that the transient can be characterized as a point source (fixed ϕ, FP, approximation) or a circle attached to Sun-center (harmonic mean, HM, approximation), respectively. These geometries constitute extreme descriptions of solar wind transients, in terms of their cross-sectional extent. Here, we present the stereoscopic expressions necessary to derive propagation direction and radial distance/speed profiles of such transients based on the more generalized self-similar expansion (SSE) geometry, for which the FP and HM geometries form the limiting cases; our implementation of these equations is termed the stereoscopic SSE method. We apply the technique to two Earth-directed CMEs from different phases of the *STEREO* mission, the well-studied event of 2008 December and a more recent event from 2012 March. The latter CME was fast, with an initial speed exceeding 2000 km s^{-1}, and highly geoeffective, in stark contrast to the slow and ineffectual 2008 December CME.

Key words: solar wind – Sun: corona – Sun: coronal mass ejections (CMEs) – Sun: heliosphere

1. INTRODUCTION

The launch of the Solar Mass Ejection Imager (SMEI; Eyles et al. 2003) onboard the Earth-orbiting *Coriolis* spacecraft, in 2003 January, pioneered truly wide-angle, white-light imaging of the inner heliosphere. Prior to this time, imaging of the solar atmosphere had, in general, been limited to within a few tens of solar radii from Sun-center. The subsequent launch, in 2006 October, of NASA's twin *STEREO* spacecraft into near 1 astronomical unit (AU) heliocentric orbits—one leading and the other lagging the Earth—heralded the advent of wide-angle, white-light heliospheric imaging (by the Heliospheric Imager, HI, instruments; Eyles et al. 2009) from a vantage point off the Sun–Earth line; this configuration was motivated, not least, by the desire to study Earth-directed coronal mass ejections (CMEs) from their inception on the Sun to their impact at Earth.

However, in attempting to ascertain the characteristics of solar wind transients observed out to large elongations (Sun-observer-transient angles), it is important to bear in mind that the relationship between their elongation angle and radial distance is highly nonlinear; it transpires that rather than being an inconvenience, the simple geometrical basis for this effect can actually be exploited to infer the kinematic properties of such transients (as discussed widely by a multitude of authors including Sheeley et al. 1999, 2008; Kahler & Webb 2007; Rouillard et al. 2008; Howard & Tappin 2009; Lugaz 2010; Möstl et al. 2011; Davies et al. 2012).

In its most simplistic form, the conversion of elongation angle to radial distance can be performed by assuming that the solar wind transient can be adequately represented as a point source, a concept originally introduced by Sheeley et al. (1999); Kahler & Webb (2007) introduced the terminology of the fixed ϕ (FP) approximation for such a geometry. The radial distance from the center of the Sun, $R_{\rm FP}$, of a point-like transient viewed along an elongation ε at a time t, by an observer situated at distance d_0 from the Sun, can be expressed in the form

$$R_{\rm FP}(t) = \frac{d_0 \sin(\varepsilon(t))}{\sin(\varepsilon(t) + \phi(t))}, \quad (1)$$

where ϕ describes the solar wind transient's angle of propagation relative to the Sun-observer line—the observer-Sun-transient angle (e.g., Sheeley et al. 1999, 2008; Kahler & Webb 2007; Rouillard et al. 2008). This equation provides the basis of the FP fitting (FPF; Rouillard et al. 2008; Sheeley et al. 2008) technique; note that the nomenclature used by Möstl et al. (2011) is mainly adopted here. Briefly, in the FPF technique, the observed time-elongation profile, $\varepsilon(t)$, of a solar wind transient viewed from a single vantage point is compared to theoretical functions governed by the inverse of Equation (1), in which $\varepsilon(t)$ is expressed in terms of propagation direction, ϕ, and radial speed, V_r (e.g., Rouillard et al. 2008; Sheeley et al. 2008). The best-fit defines the kinematic properties ascribed to the transient. Whereas the single-spacecraft FPF technique is based on the premise that ϕ and V_r remain constant over the duration of the

fitted time-elongation profile, these constraints can be relaxed if the solar wind transient is observed simultaneously from two viewpoints. The stereoscopic triangulation method—that was developed by Liu et al. (2010a, 2010b) and is based on the same point-like (FP) transient geometry as adopted in the FPF technique—enables time profiles of both ϕ, $R_{\rm FP}$ and hence V_r to be derived if simultaneous time-elongation profiles of the transient are available from two spatially separated observers.

The form of the underlying geometric model means that the aforementioned single-spacecraft FPF and stereoscopic triangulation techniques, both of which are based on the FP-type geometry, are more applicable to features that are narrow in terms of their cross-sectional extent; such analysis has been successfully applied to longitudinally restricted CMEs and most notably small-scale plasma blobs that have become entrained at the stream interface (e.g., Rouillard et al. 2008, 2010; Sheeley et al. 2008). In view of this limitation, Lugaz (2010) and Lugaz et al. (2010), respectively, embarked on single-spacecraft and stereoscopic techniques based on an alternative geometry that was considered more applicable particularly in the case of wide CMEs. The harmonic mean (HM) approximation is founded on the assumption that the cross-section of the solar wind transient can be adequately described as a circle that is attached to the center of the Sun by a point on its circumference (see, for example, Figure 1 of Möstl et al. 2011 for a schematic representation of the HM and FP geometries). For a transient that conforms to the HM geometry, the radial distance from Sun-center of its apex, $R_{\rm HM}$ (i.e., the point on the circle at the greatest distance from the Sun), at time t, is governed by the equation (Lugaz et al. 2009; Howard & Tappin 2009)

$$R_{\rm HM}(t) = \frac{2d_0 \sin(\varepsilon(t))}{\sin(\varepsilon(t) + \phi(t)) + 1}. \quad (2)$$

In this case, ϕ denotes the angle between the propagation direction of the transient's apex and the Sun-observer line, while the elongation angle ε corresponds to one of the two possible tangents from the observer's line of sight to the transient's circular form (due to their limited viewing capability, only one tangent to the HM's circumference will lie within the field of view of the HI instrument on either *STEREO* spacecraft, although this is true for a HM-type transient propagating in virtually any direction from the Sun). The single-spacecraft HM fitting (HMF) technique (Lugaz 2010; Möstl et al. 2011) is analogous to the FPF method described above, although it transpires that the inversion of Equation (2) is less trivial than is the case for the FP geometry. Two independent forms of the solutions for $\varepsilon(t)$ for a HM geometry have been derived by previous authors; the solution for $\varepsilon(t)$ derived by Möstl et al. (2011; see their Appendix A) has a single term compared with the two-termed solution derived independently by Liu et al. (2010b) and Lugaz (2010). The stereoscopic equivalent to the direct triangulation technique of Liu et al. (2010a, 2010b) based on a HM geometry—the so-called the tangent to a sphere (TAS) method—was developed by Lugaz et al. (2010), although Liu et al. (2010b) had also mooted the idea of basing a stereoscopic technique on the HM geometry. As for the HMF technique, the TAS method is founded on the assumption that the elongation along which a solar wind transient manifests itself to each observer does not correspond to the transient apex but instead to the tangent to a circle that is attached to Sun-center; as in triangulation, time profiles of both ϕ and V_r can be derived using the TAS technique if simultaneous time-elongation profiles are available from two observers. For more detailed reviews of the aforementioned techniques the reader is directed to Liu et al. (2010b) and Möstl et al. (2011).

Although the HM geometry, that underlies the HMF and TAS techniques, is clearly more appropriate than the FP geometry in the case of wide CMEs, it is clear that these two geometries constitute extreme descriptions of solar wind transients in terms of their cross-sectional extent. Lugaz et al. (2010), in their "model 2," introduced an alternative geometry in which the transient, although still circular in cross section, is not bound to the Sun. Davies et al. (2012) developed this geometry into a single-spacecraft fitting technique akin to the FPF and HMF methods, which the authors termed self-similar expansion fitting (SSEF), based on inversion of the following expression that characterizes the radial distance from Sun-center, $R_{\rm SSE}$, at time t of the transient apex for such a geometry (Davies et al. 2012; Möstl & Davies 2013—see the latter for the derivation):

$$R_{\rm SSE}(t) = \frac{d_0 \sin(\varepsilon(t))(1 + \sin(\lambda(t)))}{\sin(\varepsilon(t) + \phi(t)) + \sin(\lambda(t))}. \quad (3)$$

As distinct from Equations (1) and (2), Equation (3) includes the parameter λ, which corresponds to the transient's cross-sectional angular half width subtended at the center of the Sun, a parameter related to the curvature of its front. The so-called self-similar expansion (SSE) geometry, governed by Equation (3), can actually be regarded as a generalized geometry for which the FP and HM models form limiting cases, defined by $\lambda = 0^\circ$ and $\lambda = 90^\circ$, respectively (Davies et al. 2012; see Figures 1 of Davies et al. 2012 and Möstl & Davies 2013 for schematic representations of the SSE geometry). Note that for the SSE geometry, it is possible for both tangents to lie within the field of view of a single *STEREO*/HI instrument; in such cases, the foremost elongation should generally be used to determine the transient's apex position (see Davies et al. 2012). Although, theoretically, the single-spacecraft SSEF technique provides the potential to yield simultaneous best-fit estimates of ϕ, V_r, and λ—again on the premise that these parameters remain constant over the duration of the fitted time-elongation profile—Davies et al. (2012), through the use of Monte-Carlo simulations and from observational evidence, found that performing such a multi-variant fit with so many free parameters was largely untenable in practice. One solution that was recommended by those authors is the use of a pre-defined value of λ intermediate between the extreme values of 0° and 90° that correspond to the FP and HM cases; the selection of an appropriate value for λ could be based on previous observations or additional information specific to the event undergoing analysis.

In Section 2, below, we derive an expression equivalent to those presented by Liu et al. (2010a, 2010b) and Lugaz et al. (2010) for triangulation and TAS, respectively, that enables ϕ, $R_{\rm SSE}$ and V_r profiles to be derived from stereoscopic observations based on use of the more generalized SSE geometry with an assumed value of λ (Lugaz et al. 2010; Davies et al. 2012; Möstl & Davies 2013); note that this differs from the approach of Lugaz et al. (2010) who, when they introduced the SSE model as their model 2, developed a system of two quadratic equations to determine radial distance and radius of curvature (effectively λ) for an assumed propagation direction. The current technique is demonstrated in Section 3, through its application to two Earth-directed CMEs observed by the HI instruments on the *STEREO* spacecraft from different phases of the mission and, by virtue of that fact, from different phases of the solar cycle.

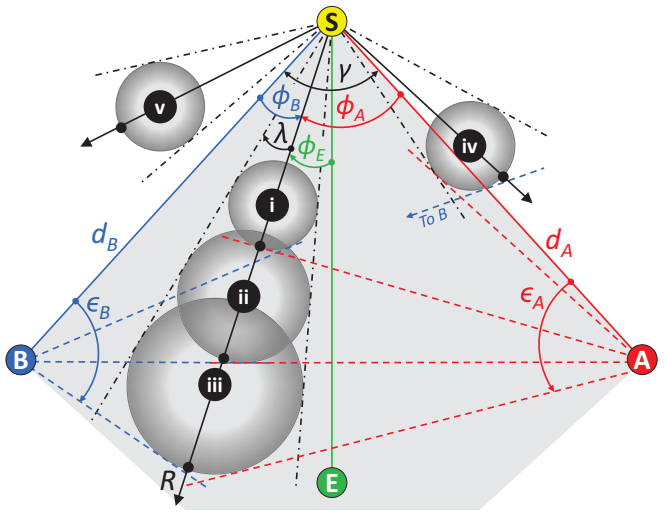

Figure 1. Schematic view (from above) of an example of the geometry described in the paper. Features i, ii, and iii illustrate three instances during the propagation of a solar wind transient—with a geometry that conforms to a self-similarly expanding circular form with constant half width, λ—traveling outward from the Sun (S) at an angle ϕ_A relative to observer A, ϕ_B relative to observer B, and ϕ_E relative to Earth (E). The two observers, located at distances d_A and d_B from the center of the Sun, are separated by an angle γ; the region where the fields of view of observers A and B overlap, for the configuration under consideration here, is shaded in gray. At each instance, dashed red and blue lines indicate the foremost elongation, ε_A and ε_B, along which the transient is visible from the positions of A and B, respectively. The small black dots indicate the location of its apex (its furthest point from the Sun, corresponding to a radial distance R). Although, for simplicity, the propagating transient (described by features i, ii, and iii) is shown to travel radially outward with a constant half width, the stereoscopic analysis technique described in this paper does not actually require either assumption to be made. While features i, ii and iii illustrate the propagation of a solar wind transient along a direction that lies within the common field of view (in this case the entire transient lies within that gray shaded region), the propagation direction of feature iv is outside the common field of view; this feature is, however, still visible to both observers in this viewing configuration. Feature v is not detectable by observer B, being wholly outside its field of view.

2. METHODOLOGY

As noted above, the stereoscopic methods of triangulation (Liu et al. 2010a, 2010b) and TAS (Lugaz et al. 2010) can be used to retrieve the kinematic properties of a solar wind transient as a function of time, as it propagates out through the inner heliosphere, based on its time-elongation profile observed simultaneously from two vantage points. The geometrical models that underlie these two techniques—namely a point-source and a circle attached to Sun-center, respectively—characterize two extremes in terms of the cross sectional extent of solar wind transients (angular half widths of $\lambda = 0°$ and $\lambda = 90°$, respectively). In this section, we derive equivalent expressions to those quoted in the aforementioned papers that can be used as the basis of an analogous, but more generalized, stereoscopic technique, based on the use of the SSE geometry (Lugaz et al. 2010; Davies et al. 2012; Möstl & Davies 2013) where any value of λ deemed appropriate can be assumed.

Such a stereoscopic analysis based on the SSE geometry is illustrated diagrammatically in Figure 1. Features i, ii, and iii represent three instances during the propagation of a solar wind transient (viewed from above)—with a geometry that conforms to a self-similarly expanding circular form with constant half width, λ—propagating outward from the Sun (S) at an angle ϕ_A relative to observer A, ϕ_B relative to observer B, and ϕ_E relative to Earth (E). The two observers, located at distances d_A and d_B from the center of the Sun, are separated by an angle γ. Although, for simplicity, the transient is shown to propagate radially outward–albeit neglecting, for the purposes of the schematic, the motion of the spacecraft during the transient's propagation—the stereoscopic analysis technique described in this paper does not require this assumption to be made. At each instance, dashed lines indicate the foremost elongation, ε_A (red) and ε_B (blue), along which the transient can be viewed from the positions of observers A and B, respectively (which are most likely to be the *STEREO-A* and *STEREO-B* spacecraft). Note that elongation is, by convention, always positive, with values up to a maximum of 180°. The elongation corresponds to the tangent to the transient's assumed circular form and is not the elongation of the apex itself (except in the case of $\lambda = 0°$). Small black dots indicate the location of the apex of the transient (at a radial distance R; note that we discard the SSE suffix from R hereafter for simplicity). Since it is likely that the following technique would mainly be applied to observations that include those from the *STEREO*/HI instrument, we define a geometry that is most applicable to this scenario, in which the shaded gray area represents the region where the fields of view of the two observers overlap (the common field of view). Features i, ii and iii illustrate the propagation of a solar wind transient along a direction that lies within the combined field of view of the two observers (in this case, the entire transient lies within that common field of view). For such an example, we define ϕ_A to be measured clockwise from the Sun–spacecraft line and ϕ_B to be measured anticlockwise from the Sun–spacecraft line. However, as discussed by such authors as Lugaz et al (2010) in terms of the TAS techniques, a transient propagating along a direction that lies outside the common field of view can still be viewed by both observers provided its circular form impinges into the common field of view (i.e., if its direction of propagation is within an angle λ of the edge of the common field of view, as in the case of feature iv in Figure 1). Feature v would not be detectable in such an observation configuration, as it lies wholly outside the common field of view. Obviously, performing a stereoscopic analysis based on the assumption that $\lambda = 0°$—i.e., corresponding to the direct triangulation approach of Liu et al. (2010a, 2010b)—would limit the transient's propagation path to a direction that lies within the common field of view. Note that, by deriving additional sets of equations pertaining to alternative configurations, Liu et al. (2010b) do cater for scenarios such as feature v within their stereoscopic triangulation approach. We choose not to do that for the current paper.

If we consider a solar wind transient conforming to the model 2/SSE geometry that can be observed simultaneously from two viewpoints (here designated A and B), we can write the following two expressions for the radial distance from Sun-center of its apex, R, based on Equation (3) and the nomenclature used in the description of Figure 1:

$$R = \frac{d_A \sin\varepsilon_A(1+\sin\lambda)}{\sin(\varepsilon_A+\phi_A)+\sin\lambda} \tag{4a}$$

and

$$R = \frac{d_B \sin\varepsilon_B(1+\sin\lambda)}{\sin(\varepsilon_B+\phi_B)+\sin\lambda}. \tag{4b}$$

These equations are valid at any instant t during the solar wind transient's propagation (although we neglect t for clarity throughout the following derivation).

Based on the above equations, and configuration, we derive below an expression for ϕ_A (alternatively this could be done for ϕ_B). The basis of this is the assumed equality of Equations (4a)

and (4b). This is exactly the same methodology that underpins the triangulation and TAS techniques. Implementation of the derived equation—which we call the stereoscopic SSE (SSSE) technique—requires a value of λ to be assumed. Performing analysis using the triangulation and TAS techniques, using the expressions given by Liu et al. (2010a; 2010b) and Lugaz et al. (2010) is, in fact, equivalent to implementing this new SSSE method with λ set to 0° and 90°, respectively.

Assuming that Equations (4a) and (4b) for the radial distance of the apex of the solar wind transient can be equated (and dividing through by $1 + \sin\lambda$) gives

$$\frac{d_A \sin\varepsilon_A}{\sin(\varepsilon_A + \phi_A) + \sin\lambda} = \frac{d_B \sin\varepsilon_B}{\sin(\varepsilon_B + \phi_B) + \sin\lambda}. \quad (5)$$

We define a variable P to be the same as that used by Lugaz et al. (2010) in their derivation of the TAS technique, such that

$$P = \frac{d_B \sin\varepsilon_B}{d_A \sin\varepsilon_A}. \quad (6)$$

Substituting P into Equation (5) yields

$$\frac{1}{\sin(\varepsilon_A + \phi_A) + \sin\lambda} = \frac{P}{\sin(\varepsilon_B + \phi_B) + \sin\lambda}. \quad (7)$$

Furthermore, we define γ as the separation angle between the two observers, subtended at Sun-center, such that

$$\gamma = \phi_A + \phi_B. \quad (8)$$

In defining γ in this way, we are limiting the technique to observations that are made in the plane that contains the two observers, which, for *STEREO*, corresponds to the ecliptic plane (in this case, ϕ_A and ϕ_B are longitude relative to spacecraft A and B, respectively, in an ecliptic-based coordinate system, with $\phi_A(\phi_B)$ being measured eastward (westward) of the corresponding Sun–spacecraft line). Note that this is also inherent in the implementations of triangulation and TAS presented by Liu et al. (2010a, 2010b) and Lugaz et al. (2010). For observations made out of that plane, this identity is no longer valid.

By defining γ in this manner, we are able to eliminate ϕ_B from Equation (7) which becomes:

$$\frac{1}{\sin(\varepsilon_A + \phi_A) + \sin\lambda} = \frac{P}{\sin(\varepsilon_B + \gamma - \phi_A) + \sin\lambda}. \quad (9)$$

The elimination of ϕ_B (equivalently ϕ_A could be eliminated in deriving an expression for ϕ_B) is pivotal in the derivation.

Standard trigonometric identities allow us to write the following expressions for $\sin(\varepsilon_A + \phi_A)$ and $\sin(\varepsilon_B + \gamma - \phi_A)$

$$\sin(\varepsilon_A + \phi_A) = \sin\varepsilon_A \cos\phi_A + \cos\varepsilon_A \sin\phi_A \quad (10a)$$

$$\sin(\varepsilon_B + \gamma - \phi_A) = \sin(\varepsilon_B + \gamma)\cos\phi_A - \cos(\varepsilon_B + \gamma)\sin\phi_A. \quad (10b)$$

These expressions can simply be substituted into Equation (9), which, after some further rudimentary rearrangement, can be expressed in the form

$$\sin(\varepsilon_B + \gamma)\cos\phi_A - \cos(\varepsilon_B + \gamma)\sin\phi_A + \sin\lambda = P\sin\varepsilon_A \cos\phi_A + P\cos\varepsilon_A \sin\phi_A + P\sin\lambda. \quad (11)$$

Separating terms containing $\cos\phi_A$ (and λ) and $\sin\phi_A$ onto opposite sides leads to the formulation

$$\cos\phi_A(\sin(\varepsilon_B + \gamma) - P\sin\varepsilon_A) + (1 - P)\sin\lambda = \sin\phi_A(\cos(\varepsilon_B + \gamma) + P\cos\varepsilon_A). \quad (12)$$

In order to simplify the remainder of the derivation, we define the parameters L, M and N, such that

$$L = \cos(\varepsilon_B + \gamma) + P\cos\varepsilon_A, \quad (13a)$$

$$M = \sin(\varepsilon_B + \gamma) - P\sin\varepsilon_A, \quad (13b)$$

and

$$N = (1 - P)\sin\lambda. \quad (13c)$$

Thereafter, substituting L, M and Ninto Equation (12) yields the simple expression

$$M\cos\phi_A + N = L\sin\phi_A. \quad (14)$$

Squaring both sides of Equation (14) leads to

$$M^2\cos^2\phi_A + 2MN\cos\phi_A + N^2 = L^2\sin^2\phi_A. \quad (15)$$

We choose to solve Equation (15) for $\cos\phi_A$—although we could equally solve for $\sin\phi_A$—by invoking the well-known trigonometric identity

$$\cos^2\phi_A + \sin^2\phi_A = 1, \quad (16)$$

such that Equation (15) can be expressed in the form

$$M^2\cos^2\phi_A + 2MN\cos\phi_A + N^2 = L^2(1 - \cos^2\phi_A). \quad (17)$$

Further rearrangement results in the following quadratic equation in terms of $\cos\phi_A$

$$(L^2 + M^2)\cos^2\phi_A + 2MN\cos\phi_A + (N^2 - L^2) = 0, \quad (18)$$

which can be solved, using the standard solution of a quadratic equation, to give

$$\cos\phi_A = \frac{-2MN \pm \sqrt{4M^2N^2 - 4(L^2 + M^2)(N^2 - L^2)}}{2(L^2 + M^2)}. \quad (19)$$

On expanding the bracketed terms under the square root, Equation (19) can be further simplified to

$$\cos\phi_A = \frac{-MN \pm L\sqrt{L^2 + M^2 - N^2}}{L^2 + M^2}. \quad (20)$$

It is important to recognize that there are two roots to a quadratic and that neither of these roots can be neglected per se, as either can be valid. However, overlooking for a moment the fact that there are two distinct roots, it also needs to be borne in mind that for each of these potential solutions there is an inherent ambiguity (between ϕ_A and $360^\circ - \phi_A$) in retrieving ϕ_A from $\cos\phi_A$ (obviously an equivalent ambiguity arises when considering $\sin\phi_A$). A transient conforming to the SSE geometry in its most extreme form (the HM form) will impinge into the *STEREO*/HI field of view irrespective of its direction of propagation, so such an ambiguity is undesirable. The ambiguity can be resolved, for each root, by simply deriving

the corresponding value of $\sin\phi_A$, and considering the respective signs of the both $\cos\phi_A$ and $\sin\phi_A$ terms.

For each of the two roots, the corresponding value of $\sin\phi_A$ can be derived from Equation (21), which is a simple rearrangement of Equation (14):

$$\sin\phi_A = \frac{M\cos\phi_A + N}{L}. \quad (21)$$

Note that if the quadratic equation had been posed in terms of $\sin\phi_A$, an equivalent rearrangement of Equation (14) would be used to yield the corresponding value of $\cos\phi_A$ for each root.

For each of the two resultant ($\cos\phi_A$, $\sin\phi_A$) combinations, $\tan\phi_A$ can be evaluated thus

$$\tan\phi_A = \frac{\sin\phi_A}{\cos\phi_A}. \quad (22)$$

Expanding Equation (22), by substituting Equations (21) and (20) for the numerator and denominator respectively, gives, with some rearrangement, the following "final" usable expressions for the "positive" and "negative" roots, respectively:

$$\tan\phi_A = \frac{LN + M\sqrt{L^2 + M^2 - N^2}}{-MN + L\sqrt{L^2 + M^2 - N^2}}, \quad (23)$$

and

$$\tan\phi_A = \frac{LN - M\sqrt{L^2 + M^2 - N^2}}{-MN - L\sqrt{L^2 + M^2 - N^2}}. \quad (24)$$

Taking into account the signs of the numerator and denominator (which are the signed parts of $\sin\phi_A$ and $\cos\phi_A$, respectively) removes any ambiguity in the derivation of ϕ_A; this can be done through the appropriate use of a two-argument four-quadrant inverse tangent function (such as the ATAN(Y, X) syntax in IDL or ATAN2(Y, X) in MATLAB). This does not, however, resolve the issue of there being two (potentially valid) solutions corresponding to the two roots of Equation (20).

Ensuring that you obtain a valid solution for ϕ_A requires that both of these roots are evaluated in all cases; fortunately, the valid solution can usually be identified based on simple physical as opposed to mathematical considerations. Even when considering a single solar wind transient propagating through the inner heliosphere, it is often necessary to select different roots for different parts of its propagation path. We find that the most robust method of identifying the valid solution, based on such physical constraints, is by deriving the corresponding time profiles of radial distance, R, and radial speed, V_r, for both roots. The radial distance can be derived by substituting values of ϕ_A into Equation (4a) and radial speed, by differentiation of the radial distance (as is done, for example, in the next section). Of course, in the limiting situation where only a single (simultaneous) estimate of elongation is available from each observer, the latter cannot be evaluated.

In many situations, the correct solution for ϕ_A can easily be identified as that which corresponds to a positive radial distance. Solutions for ϕ_A that lead to a negative radial distance correspond to the case where the radius of the solar wind transient has expanded faster than the distance from the Sun to the transient's midpoint. This equates to a scenario in which the Sun is engulfed by the transient—a non-physical solution. Note that for the positive values of $\sin\lambda$ relevant to our situation, there are no circumstances under which negative radial distances arise simultaneously for both solutions for ϕ_A. The most potentially problematic cases are those where both solutions for ϕ_A yield positive radial distances. In essence, there are two different yet potentially physically realistic solar wind transients that yield an identical combination of ε_A and ε_B. In many such cases, it is also relatively easy to identify (albeit with care) the most likely value for ϕ_A as that which provides a "physically realistic" value for the radial speed (if time profiles of elongation are available from both observers). This is because, in many of these scenarios, the ambiguity is between a faster-moving far-side transient and a slower-moving near-side transient (in particular, this scenario arises when $\gamma + \varepsilon_A + \varepsilon_B$ is smaller than the full angular width of the transient, $2 \times \lambda$). It should be reiterated that the root that corresponds to the "correct" propagation direction will likely swap over as the transient propagates outward. However, there are cases where the two solutions for ϕ_A are sufficiently similar that there is no obvious way to discern which the most likely; they yield similar radial distances and, hence, speed. However, the fact that they are so similar does mean that it is likely that they both lie within the errors induced by the underlying assumptions (such as the transient being circular). There are also very specific cases where ϕ_A is undefined, in particular when $\varepsilon_A + \varepsilon_B + \gamma = 180^\circ$ (scenario ii in Figure 1), where a unique solution for ϕ_A is not possible as the tangential lines of sight from the two observers to the model transient coincide along their entire length (note this is an equivalent condition to $P = 0$). It should be borne in mind that as $\varepsilon_A + \varepsilon_B + \gamma$ approaches 180°, small observational errors in elongation will yield large errors in ϕ_A. Note that if an observer subsequently emerges from inside the solar wind transient—in the case where the transient has completely passed over the observer—the derived equations are no longer applicable as Equations (4a) and (4b) pertain to the apex of the transient and not its trailing point (see Davies et al. 2012).

Application of the aforementioned derivation to feature iv in Figure 1 would likely yield a negative value of ϕ_A (as, in most programming languages, two-argument four-quadrant inverse tangent functions output values between -180° and $+180^\circ$). However the derivation is not applicable to transients such as feature v that do not encroach into the common field of view of the two observers. However, coronagraphs (and indeed the SMEI instrument) are not subject to the limitations in the angular extent of the field of view suffered by the *STEREO*/HI instrument. The preceding derivation could be modified to deal with such situations, as was done by Liu et al. (2010b) for the triangulation technique, although the *STEREO*/HI-oriented coordinate system used in the current paper is not ideal.

In the limiting FP case, where $\lambda = 0^\circ$, Equations (23)/(24) simplify (albeit with slight rearrangement) to the direct triangulation expression derived by Liu et al. (2010a, 2010b). In the case of a single point-like transient, there are no longer two "real" roots, but the use of Equations (23) and (24), and then selecting ϕ_A on the basis of a positive radial distance, will ensure that the appropriate value of ϕ_A is extracted at any point along the transient's propagation path. It is not as trivial to demonstrate the equivalence of the above derivation with Lugaz et al.'s (2010) original TAS formulation for the case of $\lambda = 90^\circ$, as those authors actually solved for what we call ϕ_E (they simply call it ϕ), which is the direction of propagation of the transient relative to the Sun–Earth line (rather than being relative to one of the observing spacecraft). For completeness, we present in Equation (25) below the necessary adaptation of Lugaz et al.'s (2010) original formulation (their Equation (2)) that is required to account for the SSE geometry. This inclusion of Equation (25)

is simply for the benefit of those already using that formulation and we make no comment on the regimes of its validity as we have done for the expression derived in this paper.

In its revised form, ϕ_E(Equation (2) of Lugaz et al. 2010) can be expressed as

$$\phi_E = \sin^{-1}\left(\frac{P-1}{Q}\sin\lambda\right) + \alpha. \quad (25)$$

Readers are directed to Lugaz et al. (2010) for an explanation of the use of this formulation, but its amendment to cater for the SSE geometry simply involves the inclusion of sin λ within the inverse sine term.

Equations (23) and (24) form the basis of the SSSE technique, in which we derive ϕ_A as a function of time based on an assumed value of λ; there is no absolute requirement for that assumed value of λ to be kept constant with time, although not doing so defies the concept of SSE. The SSSE technique is demonstrated in the subsequent section, based on heliospheric images of two Earth-directed CMEs observed by the *STEREO* spacecraft.

3. APPLICATION

In the previous section, we derived an methodology for deriving the instantaneous propagation direction (ϕ_A, the angle from observer A) of the apex of a circular solar wind transient, characterized by a half width λ, in terms of the elongation angle of that feature viewed simultaneously from two vantage points (here given by ε_A and ε_B). Except in the case of $\lambda = 0°$, these elongations correspond not to the apex itself (except for very fleeting geometries akin to feature ii in Figure 1 as viewed from observer A), but to the tangent to the transient's assumed circular form. Having derived the propagation direction, the corresponding value of the radial distance of the apex of the circular transient can be evaluated, using Equation (4a). Continuous monitoring of the solar wind transient from two view points enables the time profile of its propagation direction and radial distance (and, hence, radial speed as the time derivative of the latter) to be derived, as the feature propagates out through the inner heliosphere; this concept forms the basis of what we term the SSSE technique.

In this section, we demonstrate the SSSE technique based on *STEREO*/HI observations of two near-Earth directed CMEs from very different phases of the mission. The first of these CMEs (CME 1), which was launched at around 08 UT on 2008 December 12, has been rigorously studied through the application of the aforementioned techniques by such authors as Liu et al. (2010a, 2010b), Davis et al. (2009) and Lugaz et al. (2010); this was not least due to it being the first Earth-impacting CME of the *STEREO* era that was imaged simultaneously from vantage points well outside the Sun–Earth line (*STEREO-A* and *STEREO-B* were separated from the Sun–Earth line by some 42° and 44°, respectively). Thus it is an obvious candidate for consideration here. The second, much more recent, CME (CME 2)—launched at around 00 UT on 2012 March 7—was imaged by the two *STEREO* spacecraft from vantage points some 110° (*STEREO-A*) and 118° (*STEREO-B*) from the Sun–Earth line. By virtue of its significant speed, this CME was associated with a major solar energetic particle (SEP) event that was observed both in the vicinity of Earth and at the *STEREO-B* spacecraft itself. For each of these two CMEs, Figure 2(a) presents a pair of near-simultaneous difference images from the HI-1 instruments on *STEREO-A* (HI-1A) and *STEREO-B* (HI-1B); difference images of CME 1 and CME 2 are from 06:49 UT on 2008 December 13 and 07:29 UT on 2012 March 7, respectively (the time being that of the "current" as opposed to the "previous" image of the image pair). The near-horizontal line that runs across the center of each difference image corresponds to the projection of the ecliptic plane onto the image plane, as viewed by the observing spacecraft.

Figure 2(b) presents the time-elongation profiles of the foremost density front of each CME rendered in white light from *STEREO-A*/HI (red line) and *STEREO-B*/HI (blue line). The profiles are extracted manually from ecliptic time-elongation maps (commonly called J-maps) created from combined HI-1 and HI-2 difference observations (e.g., Davies et al. 2009). As in the other studies of this type, it is the interface between the adjacent white and black regions (that, between them, constitute the signature of a solar wind transient, such as a CME, in a difference J-map) that is tracked; while this interface corresponds to a somewhat arbitrary location within the density feature, its heightened contrast leads to a better defined time-elongation profile (as discussed by Lugaz et al. 2012). The time-elongation profile of CME 2, as viewed from *STEREO-B*, is curtailed near 06 UT of March 8 by the onset of contamination in the HI images by the SEP event.

Figure 2(c) presents ϕ_A as a function of time for the initial front of each CME, based on the application of the SSSE technique (through the use of Equations (23) and (24)) to the time-elongations illustrated in Figure 2(b). While the absolute scale over which ϕ_A is plotted is different for the two CMEs, the angular range is the same for both. For both CMEs, the time profile of ϕ_A is evaluated for 10 values of λ ranging from 0° (black) to 90° (red) in steps of 10°. Note that in these and subsequent panels, and in particular for the larger values of λ, convergence of the derived parameters result in not all individual traces being easily discernable. The requirement for simultaneous values of elongation from the two observers necessitates that the time-elongation profiles be interpolated onto a common time grid, here at 30 minute resolution (even though HI images from the two spacecraft are contemporaneous, this simultaneity is lost by the manner in which the time-elongation profiles are extracted from the J-maps). At each point in time, heliocentric distances of *STEREO-A* and *STEREO-B*, d_A and d_B respectively, and their angular separation, γ,are retrieved from the spacecraft ephemeris data; note that in the case of CME 2, the value of γ that should be used is 228° (as opposed to 132°). In the case of CME 1, the positive root defined by Equation (23) is appropriate throughout, while for CME 2, the negative root (Equation (24)) is appropriate. While the correct solution is, in the main, easily determined through selection based on the sign of the radial distance (i.e., selecting the positive radial distance), for CME 1, in particular, there are regimes over which both roots yield a positive radial distance (corresponding to higher values of λ). Over these regimes, the incorrect root is obvious as it is associated with wholly ridiculous values of the radial distance and derived radial speed. As noted previously, for the configuration of the *STEREO* mission, ϕ_A corresponds to the ecliptic longitude of propagation of the transient relative to the *STEREO-A*; Figure 2(d) presents the propagation angle as a longitude relative to Earth, ϕ_E (i.e., HEE—Heliocentric Earth Ecliptic—longitude, equivalent to Stonyhurst heliographic longitude). Negative and positive values of ϕ_E correspond to propagation eastward (behind) and westward (ahead) of the Sun–Earth line.

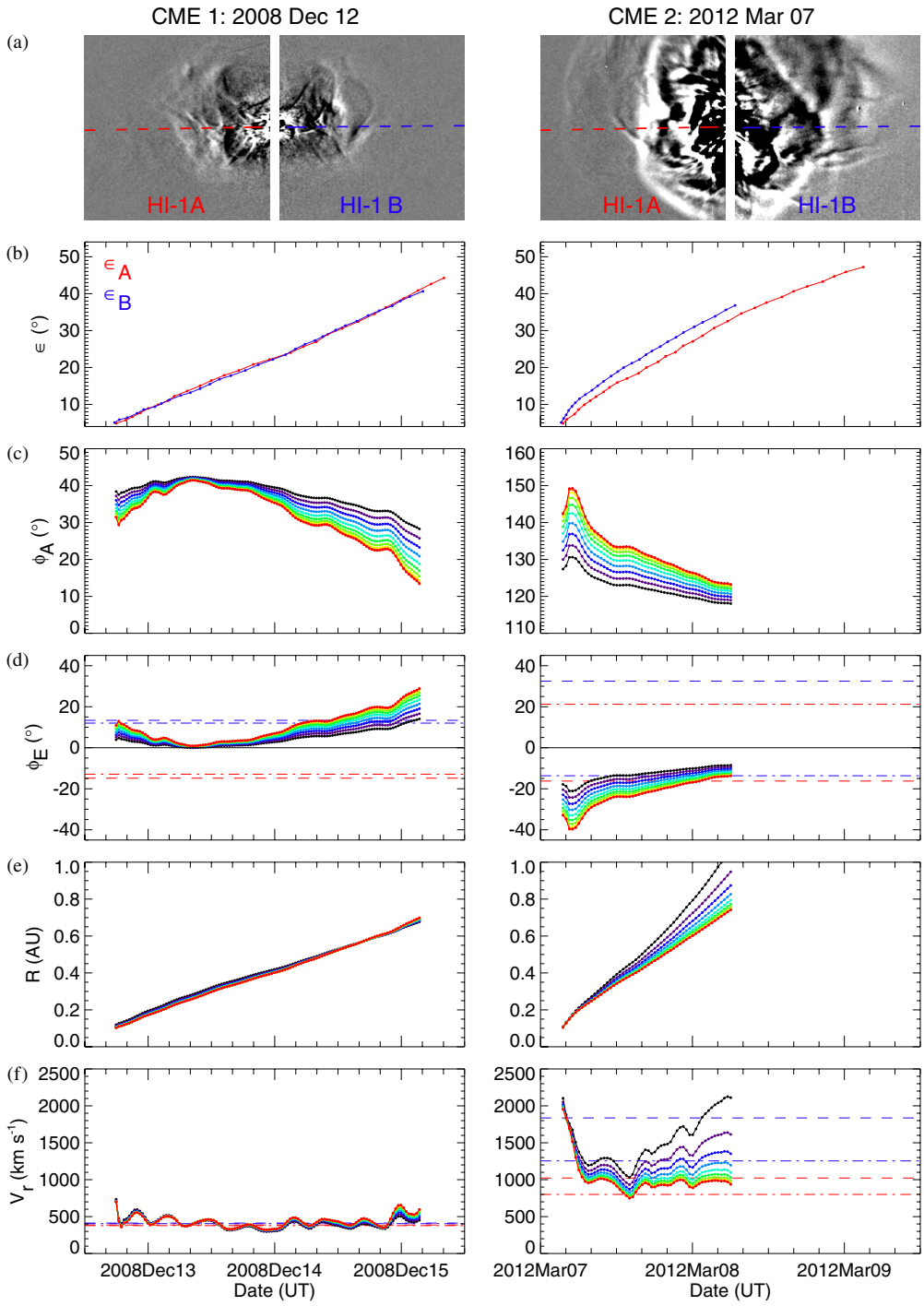

Figure 2. Results of the application of the SSSE technique to two near-Earth directed CMEs observed by the HI instruments on the *STEREO* spacecraft. These CMEs were launched at around 08 UT on 2008 December 12 (CME 1: left hand column) and 00 UT on 2012 March 7 (CME 2: right hand column). (a) Near-simultaneous HI-1A and HI-1B difference images from 06:49 UT on 2008 December 13 (CME 1) and 07:29 UT on 2012 March 7 (CME 2). The near-horizontal lines in each image correspond to the projection onto the image plane of the ecliptic plane. (b) Elongation, as a function of time, of the initial density front of each CME, as viewed in the ecliptic by the HI instrument on *STEREO-A* (red) and *STEREO-B* (blue); the time-elongation profiles are extracted manually from ecliptic time-elongation maps created by combining HI-1 and HI-2 difference observations. (c and d) Propagation angle as a function of time of the leading front of each CME relative to *STEREO-A* (ϕ_A, panel (c)) and Earth (ϕ_E, panel (d)), derived from SSSE analysis of the time-elongation profiles illustrated in panel (b) for 10 values of half width λ, the latter increasing from 0° (black) to 90° (red) in steps of 10° (in these and subsequent panels, individual traces are not easily distinguishable—in particular for larger values of λ). (e and f) Corresponding radial distance, R, and radial speed, V_r, time profiles for each of the two CMEs. For comparison, dashed and dot-dashed horizontal lines (overlaid on panels (d) and (f) only) indicate corresponding results from single-spacecraft FPF and HMF analysis, respectively, performed on the time-elongation profiles from *STEREO-A* (red) and *STEREO-B* (blue).

Application of the SSSE technique strongly suggests that, based on their ecliptic signatures, each of these CMEs is propagating in a near-Earthward direction (Figure 2(d)), although along a central axis that is (generally) westward of the Sun–Earth for CME 1 and eastward of the Sun–Earth line for CME 2 (Figure 2(d)). In the case of CME 1 in particular, it is evident that there is a situation in which propagation direction, yielded by SSSE analysis over the entire range of possible λ

values, converges to a single value of ϕ_A(Figure 2(c)). As the dependence on λ is lost when N becomes zero, this convergence arises when $P = 1$ (see Equation (13c)). For the simple case of $d_A = d_B$, this convergence corresponds to the situation where $\phi_A = \phi_B$ (i.e., the transient propagates along a direction midway between the two observers). For the *STEREO* mission configuration, convergence occurs when ϕ_E is close to—but not exactly—0° (Figure 2(d)), with Earth being roughly midway between the two *STEREO* spacecraft, and d_A and d_B being similar. As the transient's propagation path deviates from being near-Earth directed, the value of ϕ_A output by SSSE analysis becomes increasingly dependent on the choice of λ (by up to 20° in the cases we show here). This is notwithstanding the convergence of ϕ_A (and indeed all derived parameters) with increasing λ. As a transient propagates even further from the Sun–Earth line (we limit ourselves somewhat in this regard by our choice of events), the disparity in ϕ_A between the extreme cases of $\lambda = 0°$ and $\lambda = 90°$—which correspond to triangulation and TAS—will presumably become increasingly significant; in some ways, it is these cases that justify the adoption of the more appropriate "intermediate" SSSE approach. The fact that the SSSE technique—for the *STEREO* configuration at least—yields a propagation direction that becomes progressively further from the Earthward propagation direction with increasing half width λ, is in agreement with the conclusions of Lugaz (2010), drawn from comparison of results from triangulation and TAS analyses. For CME 1, the results of our SSSE analysis for $\lambda = 0°$ can be directly compared to those presented by Liu et al (2010a, their Figure 4) and by Liu et al. (2010b, their Figure 9). Given that there will invariably be subtle differences in the manner in which the methodologies are implemented here and by those authors, the propagation directions yielded by SSSE analysis with $\lambda = 0$ and by triangulation are remarkably consistent. It should be noted that Liu et al. (2010a) assumed $d_A = d_B$—a simplification that was neither made here or by Liu et al. (2010b)—which, in fact, makes a significant difference to the propagation angle derived at large elongations. Note also that, in addition to *STEREO*/HI observations, the time-elongation profiles of Liu et al. (2010a, 2010b) also included *STEREO* coronagraph (COR-2) observations; such an approach would be equally valid with the SSSE technique. Lugaz et al. (2010) also performed stereoscopic analysis of CME 1; the authors quote propagation directions of $\phi_E = 0° \pm 5°$ for triangulation and $\phi_E = 10° \pm 10°$ for the TAS technique which are not inconsistent with the results shown in Figure 2(d) for $\lambda = 0°$ and $\lambda = 90°$, respectively. In a recent paper, Liu et al. (2013) present kinematic analyses of three CMEs from early 2012, including the CME that we call CME 2. In their paper, the authors compare the results of both triangulation and TAS analysis, based on COR-2 and HI imagery, with in situ measurements and observations of type II radio bursts. Again, the propagation directions yielded by their analysis (Liu et al. 2013, their Figure 12) are agreeably consistent with what is presented in the current paper for the appropriate value of λ. As the aim of the current paper is simply to present an initial demonstration of the SSSE technique, we forgo error analysis. When applying this technique in earnest, a robust error analysis, such as detailed Liu et al. (2010b), is obviously advisable.

For each CME, Figure 2(e) presents the corresponding radial distance (R) profile of its apex, derived as a function of time for each of the ten values of λ using Equation (4a). While the selected value of λ makes very little difference to the derived radial distance profile for CME 1, this is not true for CME 2, particularly at greater elongations, presumably due to its larger propagation angle relative to the observer. Based on adjacent values of the radial distance, and their associated times, a numerical differentiation with three-point Lagrangian interpolation is used to derive the time profile of the radial speed, V_r, for both CMEs (Figure 2(f)). The speed profile derived in this manner is for the transient's apex; formulae presented by Möstl & Davies (2013) can be used to correct V_r (and hence arrival times) to account for impact of the solar transient at locations away from the transient apex. We know CME 2 to be much faster than CME 1; this is borne out by the results of the SSSE analysis. It is noticeable, however, that varying λ has a much more significant effect on the output speed for CME 2 (as would be expected from examining the corresponding profiles of R); this is a direct result of the different observing geometries for the two CMEs, as explained in detail by Liu et al. (2013). Our analysis of CME 1 confirms previous work (e.g. Liu et al. 2010a, 2010b, 2012) that shows that, for such "front-sided" Earth-directed solar wind transients, there is little difference in the radial distance and speed derived using triangulation and TAS, despite the fact that these characterize total extremes in terms of the assumed geometry. The initial rapid deceleration of CME 2 suggested by this analysis, for all values of λ, is as would be anticipated for such a fast CME. Inclusion of the COR-2 observations by Liu et al. (2013), in fact, reveals an earlier acceleration phase for this and, indeed, the other two similarly fast CMEs considered by those authors. Liu et al. (2013) suggest that the "unphysical" late acceleration yielded by the triangulation techniques for all three of their fast CMEs, including our CME 2 (see Figure 2(f)), provides evidence that these CMEs are better represented, but only when further from the Sun, by a HM geometry. Conversely, by comparing to possible source location, the authors suggest that the FP geometry may be more applicable to these CMEs when they are close to the Sun. The present work provides the capability of assigning an intermediate angular width to a solar wind transient; this may assist in enabling consistency between different datasets to be achieved in studies of that type.

Out of interest, we performed SSEF analysis on the ecliptic time-elongation profiles displayed in Figure 2(b)—exactly as implemented by Davies et al. (2012)—in order to compare results from the stereoscopic SSSE analysis to results from the analogous single-spacecraft fitting technique. The latter was applied independently to the profiles from the *STEREO-A* and *STEREO-B* spacecraft, for λ ranging from 0° to 90° in steps of 10°. Dashed and dot-dashed lines (overlaid on Figures 2(d) and (f) only) indicate SSEF results for $\lambda = 0°$ (effectively FPF) and $\lambda = 90°$ (HMF) only, for *STEREO-A* (red) and *STEREO-B* (blue); results for these values of λ essentially encompass the entire possible range of values of direction and speed that can be produced by SSEF analysis. For CME 1, the application of the SSEF technique to the time-elongation profile from *STEREO-A* (*STEREO-B*) observations yielded values of ϕ_E that rotated from −13° to −15°(+12° to +14°), and values of V_r that increased from 378 to 387 km s^{-1}(404 to 413 km s^{-1}) as λ was increased from 0° to 90°. For CME 2, corresponding values from *STEREO-A* (*STEREO-B*) are +21° to −16° (−13° to +32°) for ϕ_E, and 800 to 1022 km s^{-1} (1254 to 1836 km s^{-1}) for V_r (note that for *STEREO-B*, in particular, some values lie outside the limits of the respective plot). As is the case for the stereoscopic analysis, the best-fit parameters retrieved from the single-spacecraft analysis of CME 1 are much less sensitive to changes in λ than for CME 2. Note also that these results compare well with

equivalent values quoted by Davis et al. (2009) and Lugaz et al. (2010). For CME 1, SSEF analysis of the *STEREO-B* time-elongation profile yields results that are highly consistent with those from the SSSE technique, both in terms of propagation direction and speed; this is not the case for *STEREO-A* (for propagation direction, in particular). For CME 2, the SSSE-determined propagation angles largely fall outside the range of those derived using the SSEF technique, despite a substantial spread in the latter. However, our naive application of the SSEF technique to the time-elongation profiles of CME 2 shown in Figure 2(b) is likely to yield somewhat inaccurate results due to the likely initial deceleration of such a fast CME (borne out by the SSSE results), and, in the case of *STEREO-B*, the rather more limited profile extent (e.g., Davies et al. 2012, and references therein).

In this section, we have demonstrated the stereoscopic SSSE technique, through application to two near-Earth directed CMEs. The results of this technique appear consistent with previously published stereoscopic work (where available and applicable), but somewhat less consistent with values gleaned from single spacecraft analysis techniques—this is not least because the results from single-spacecraft analyses are not consistent in themselves. While it is not the aim of the current paper to pass judgment on the validity of the various techniques, it is worth mentioning that for these CMEs at least, the general propagation direction with respect to the Sun–Earth line gleaned from stereoscopic, as opposed to single-spacecraft analysis—irrespective of the precise value of λ used in the former—is more consistent with what the sense of the asymmetry in coronagraph images from the near-Earth *Solar and Heliospheric Observatory* spacecraft would lead us to believe.

4. SUMMARY

Recent advances in wide-angle imaging of the corona and inner heliosphere have led to the development of a plethora of techniques that enable the key kinematic properties of solar wind transients to be estimated; the launch of the *STEREO* mission, in particular, has unlocked the potential for the development of multi-spacecraft analysis techniques, based on its capability for coronal and heliospheric imaging from spatially separated vantage points. By necessity, in the current paper (Section 1), we have restricted our discussion to a limited number of closely related single-spacecraft and stereoscopic geometrical modeling techniques. Of the numerous techniques that exist for the analysis of the propagation and evolution of solar wind transients based on white-light imaging, many others are also based on the adoption of a geometrical formulation for the transient's topology, some invoke forward or magneto-hydrodynamic modeling, some rely on polarization measurements and are thus, currently, only applicable to coronagraph imagery, and others incorporate intensity measurements. We do not attempt to provide an exhaustive list here but, instead, refer the reader to a number of works in which multiple techniques have been employed or reviewed (Mierla et al. 2010; Davis et al. 2011; Webb & Howard 2012; Webb et al. 2013).

This avenue of research is of great importance to those wishing to mitigate the potentially deleterious effects of space weather, especially when the techniques can be shown to be both quickly and easily implementable and, of course, provide demonstrably reliable results. Two such methods—triangulation (Liu et al. 2010a, 2010b) and the TAS method (Lugaz et al. 2010)—can be used to determine time profiles of the propagation direction and radial speed of a solar wind transient, effectively based on comparing its elongation profile as viewed by two observers. The geometries on which these two techniques are based—a point source and a circle attached to Sun-center, respectively—constitute extreme descriptions of solar wind transients. In this paper, we derive the expressions that underpin a more generalized technique, which we call the SSSE method. Although still based on the assumption of a circular transient geometry, the SSSE technique provides more flexibility in characterizing the transient's cross-sectional extent (through defining its half width λ). Effectively, this technique generalizes the triangulation and TAS techniques, which form the limiting cases of the SSSE technique that correspond to λ of 0° and 90°, respectively.

For demonstration purposes, we apply the SSSE technique to two CMEs from different phases of the *STEREO* mission, the well-studied event of 2008 December and a more recent event from early 2012. While the selection of two CMEs that propagate close to the Sun–Earth line may not fully demonstrate the full potential of having the capability to define λ (both CMEs propagate in a regime where the retrieved propagation direction is less dependent on λ), they provide somewhat more scope in terms of inter-comparison and validation against previously published work. The work documented here is not, however, intended to be a rigorous comparison of the various techniques; rather the intent is to introduce a simple methodology for performing stereoscopic analysis that allows more flexibility than is currently available. While the stereoscopic SSSE technique, as currently implemented, is limited to the plane defined by the Sun and the two observers—this being the ecliptic plane in the case of *STEREO*—the possibility exists for the technique to be extended to consider propagation out of this plane by assuming a spherical geometry.

The authors gratefully acknowledge financial support from the UK Space Agency. *STEREO*/HI was developed by a consortium comprising Rutherford Appleton Laboratory, and University of Birmingham (UK), Centre Spatiale de Liège (Belgium), and the Naval Research Laboratory (USA). The authors acknowledge the *STEREO*/HI Principal Investigator team, within RAL Space, and the UK Solar System Data Centre, respectively, for the processing and subsequent provision of the *STEREO*/HI data. The research leading to these results has received funding from European Commission's Seventh Framework Programme (FP7/2007–2013) under grant agreement numbers 263252 (COMESEP: C.M.), 284461 (eHEROES: K.S.) and 263340 (SWIFF: K.S.). The research of C.M. was also supported by an FP7 Marie Curie International Outgoing Fellowship. N.L. was supported by grant NNX13AH94G. Y.L. was supported, in part, by the SPORT project under grant Y129164CBS and the Specialized Research Fund for State Key Laboratories of China.

REFERENCES

Davies, J. A., Harrison, R. A., Perry, C. H., et al. 2012, ApJ, 750, 23
Davies, J. A., Harrison, R. A., Rouillard, A. P., et al. 2009, GeoRL, 36, L02102
Davis, C. J., Davies, J. A., Lockwood, M., et al. 2009, GeoRL, 36, L08102
Davis, C. J., de Koning, C. A., Davies, J. A., et al. 2011, SpWea, 9, S01005
Eyles, C. J., Harrison, R. A., Davis, C. J., et al. 2009, SoPh, 254, 387
Eyles, C. J., Simnett, G. M., Cooke, M. P., et al. 2003, SoPh, 217, 319
Howard, T. A., & Tappin, S. J. 2009, SSRv, 147, 31
Kahler, S. W., & Webb, D. F. 2007, JGRA, 112, A09103
Liu, Y., Davies, J. A., Luhmann, J. G., et al. 2010a, ApJL, 710, L82
Liu, Y., Thernisien, A., Luhmann, J. G., et al. 2010b, ApJ, 722, 1762
Liu, Y. D., Luhmann, J. G., Lugaz, N., et al. 2013, ApJ, 769, 45

Liu, Y. D., Luhmann, J. G., Mostl, C., et al. 2012, ApJL, 746, L15
Lugaz, N. 2010, SoPh, 267, 411
Lugaz, N., Farrugia, C. J., Davies, J. A., et al. 2012, ApJ, 759, 68
Lugaz, N., Hernandez-Charpak, J. N., Roussev, I. I., et al. 2010, ApJ, 715, 493
Lugaz, N., Vourlidas, A., & Roussev, I. I. 2009, AnGeo, 27, 3479
Mierla, M., Inhester, B., Antunes, A., et al. 2010, AnGeo, 28, 203
Möstl, C., & Davies, J. A. 2013, SoPh, 285, 411
Möstl, C., Rollett, T., Lugaz, N., et al. 2011, ApJ, 741, 34
Rouillard, A. P., Davies, J. A., Forsyth, R. J., et al. 2008, GeoRL, 35, L10110
Rouillard, A. P., Davies, J. A., Lavraud, B., et al. 2010, JGRA, 115, A04103
Sheeley, N. R., Jr., Herbst, A. D., Palatchi, C. A., et al. 2008, ApJ, 675, 853
Sheeley, N. R., Jr., Walters, J. H., Wang, Y.-M., & Howard, R. A. 1999, JGR, 104, 24739
Webb, D. F., & Howard, T. A. 2012, LRSP, 9, 3
Webb, D. F., Möstl, C., Jackson, B. V., et al. 2013, SoPh, 285, 317